Polyhedral Crystal Films of Covalent Organic Frameworks

Xiansong Shi,[a,†] Qixing Liu,[a,†] Haipei Shao,[b] Chengjun Kang,[a] He Li,[a] Wen-Hua Li,[a] Anwesha Mukherjee,[a] Junyu Ren,[a] Nengxiu Zhu,[a] Wei Zhao,[a] Dongchen Shi,[a] Zhaoqiang Zhang,[a] Yong Wang,[c] Ming Lin,[b] and Dan Zhao[a,d,e,]*

[a]Department of Chemical and Biomolecular Engineering, National University of Singapore, 4 Engineering Drive 4, Singapore 117585, Singapore

[b]Institute of Materials Research and Engineering (IMRE), Agency for Science, Technology and Research (A*STAR), 2 Fusionopolis Way, Innovis #08-03, Singapore 138634, Singapore

[c]School of Energy and Environment, Southeast University, Nanjing, 210096, Jiangsu, P. R. China

[d]Centre for Hydrogen Innovations, National University of Singapore, 1 Engineering Drive 3, Singapore 117580, Singapore

[e]National University of Singapore (Suzhou) Research Institute, Suzhou, 215123, Jiangsu, P. R. China

E-mail: chezhao@nus.edu.sg

[†]These authors contributed equally to this work.

Abstract

Porous crystal films offer great potential for tackling energy and environmental challenges. However, despite over a decade of intensive research, covalent organic framework (COF) films exhibiting polyhedral textures reflective of their crystalline nature remain exceedingly rare. Here we present a scalable and adaptable biphasic strategy to fabricate pyrene (Py)-COF polyhedral crystal films with exceptional crystalline order under ambient conditions. This method enables precise control over polycrystal formation in solution and crystal growth on substrates, yielding Py-COF polyhedral films with tunable nanometer-scale thicknesses on a 4-inch wafer scale. Among them, a Py-1P film achieves a record-high Brunauer-Emmett-Teller surface area reported for COF films with comparable pore sizes, alongside remarkable chemical stability. Real-space electron microscopy elucidates previously undisclosed details underlying COF crystal film growth. These polyhedral crystal films show anisotropic thermal flexibility along the [001] lattice direction, with dynamically adaptive thermal expansion coefficients of 1.64-2.15 × 10^{-4} K^{-1}. Through sensor testing, we correlate polyhedral film crystallinity with device performance and longevity. This research expands the boundaries of COF films and reveals tremendous possibilities to advance film science and applications.

Introduction

Crystalline materials, renowned for their ordered atomic arrangements and exceptional physicochemical properties, have revolutionized modern materials science.[1,2] Examples such as graphene,[3] perovskites,[4] and periodic frameworks[5] have captivated global attention for their unusual structures and pathbreaking applications, spanning fields from electronics to energy storage. Among these, inherently porous crystals stand out for their well-defined pore networks and extraordinary porosity, which are unattainable in amorphous or nonporous counterparts.[6]

Metal-organic frameworks (MOFs) and covalent organic frameworks (COFs), engineered according to the principles of reticular chemistry, exemplify the class of porous crystals.[7-10] Their periodically ordered structures, customizable channels, and permanent porosity permit efficient and selective mass transport, making them invaluable for catalysis, separation, and energy conversion applications.[11-13] In response to growing global demands for sustainable energy and environmental solutions, MOFs and COFs have emerged as prime candidates for film and membrane technologies, where their potential can be harnessed for real-world applications.[14-18] MOFs, with flexible and less directional coordination bonds, readily accommodate structural reorganization and defect correction, facilitating the development of crystal-intergrown polycrystalline films.[19] COFs, however, built from robust and typically less reversible covalent bonds, face substantial challenges in achieving films with comparable crystallinity and structural coherence.[20,21] Although recent breakthroughs have yielded two-dimensional (2D) and three-dimensional (3D) single-crystal COFs for structural deciphering,[22-24] their translation into high-quality films remains limited.

Despite these hurdles, COF membranes/films have shown considerable promise in separation science,[25-29] particularly in overcoming traditional trade-offs between selectivity and permeability. Precise control over pore structures

and versatile functionalization of the pore environment position COFs as compelling candidates for next-generation membranes in desalination,[30] molecular sieving,[31,32] and gas purification[33]. However, even after a decade of intensive research, COF membranes/films with polyhedral textures that truly reflect their crystalline nature remain unexplored. This limitation raises critical concerns about the structural quality and performance of COF membranes,[20,34] as insufficient crystallinity and structural disorder often undermine their practical utility. Moreover, structural determination of COF films through definitive techniques such as X-ray diffraction and gas sorption is still underreported, particularly for those designed for separation applications.[35] More critically, efforts to elevate the quality of COF films to embody their crystal nature have been extremely limited.[21] While crystallinity is often recognized as a key determinant of performance and longevity in crystalline materials, its precise role in influencing the efficacy and stability of COF films remains unclear. Addressing these gaps necessitates not only the development of veritable COF crystal films but also a comprehensive understanding of their growth mechanisms and structure-performance correlations.

Here, we develop polycrystals and polyhedral crystal films of 2D pyrene (Py)-COFs using a scalable and adaptable biphasic method under ambient conditions. This approach allows confined crystal growth of Py-COFs on various substrates, producing large-size, thickness-controllable polyhedral crystal films that were previously considered unattainable. Comprehensive characterizations, including X-ray diffraction and N_2 sorption, reveal their exceptional crystallinity, pronounced microporosity, and robust chemical stability. Electron microscopy provides a real-space understanding of the polyhedral crystal film growth. Notably, the developed Py-COF polyhedral films exhibit unique anisotropic thermal flexibility, characterized by linear, positive thermal expansion along the [001] crystal direction. Using a sensor platform, we disclose the role of film crystallinity in improving device performance and lifespan. This research not only paves the way for fabricating COF crystal films

but also elucidates their growth mechanisms and crystallinity-performance correlations, expanding the boundaries of COF film science.

Results

Py-COF polycrystals

We synthesized polycrystals of the imine-linked Py-1P[36] framework through Schiff-base condensation between 1,3,6,8-tetrakis(4-aminophenyl)pyrene ($Py(NH_2)_4$, node) and terephthalaldehyde (TPA, linker) under ambient conditions (Fig. 1a). To achieve this, we developed a biphasic synthesis approach, where an aqueous solution of acetic acid (AcOH) was layered over a dichloromethane (DCM) solution containing the node and linker (Supplementary Fig. 1). This configuration allowed AcOH to diffuse slowly from the aqueous to the organic phase, catalyzing nucleation and crystallization of Py-1P-a-b in DCM, where a and b denote the AcOH molarity (mol L^{-1}, M) and synthesis time (h), respectively. Fourier-transform infrared (FTIR), Raman, and solid-state ^{13}C nuclear magnetic resonance (NMR) spectra verified the characteristic imine bonds in Py-1P-6-72 (Supplementary Figs. 2-4). Powder X-ray diffraction (PXRD) results validated high crystallinity of Py-1P-6-72 (Supplementary Fig. 5), together with thermal stability up to 370 °C in N_2 (Supplementary Fig. 6). FTIR spectra revealed an identical chemical composition for Py-1P-6-72 and Py-1P produced from a solvothermal method (Supplementary Fig. 7). However, scanning electron microscopy (SEM) tests recognized obvious differences in their morphologies. Py-1P-6-72 exhibited a polyhedrally textured, sphere-shaped morphology with diameters ranging from 700 to 1000 nm (Fig. 1b and Supplementary Fig. 8), whereas the solvothermal method resulted in irregular particle aggregates (Supplementary Fig. 9). PXRD and 77 K N_2 sorption results identified enhanced crystallinity and microporosity of Py-1P-6-72, despite its room-temperature synthesis (Supplementary Figs. 10-11). Transmission electron microscopy (TEM) images visualized sharp-edged polyhedral structures in Py-1P-6-72 (Fig. 1c and Supplementary Fig. 12).

Low-dose high-resolution TEM (HRTEM) images showed interlaced lattice fringes, with an inter-lattice spacing of ~2.2 nm, referring to the distance of Py-1P (110) planes (Fig. 1d and Supplementary Fig. 13). These morphological and structural characteristics manifest the formation of Py-1P-6-72 polycrystals. We examined the chemical stability of Py-1P-6-72 and found minimal changes in its morphology, weight, crystallinity, and microporosity after prolonged exposure to solvents, boiling water, and 6 M NaOH and HCl solutions (Supplementary Figs. 14-17). Beyond Py-1P, this biphasic strategy proved applicable to Py-COFs constructed from $Py(NH_2)_4$ and various dialdehyde linkers (Supplementary Figs. 18-19). These Py-COF polycrystals consistently exhibited high crystallinity, microporosity, and thermal stability (Supplementary Figs. 20-22).

Time-resolved SEM analysis was performed to probe the growth of Py-1P polycrystals, revealing a transition from clustered particles to textured spheres (Supplementary Fig. 23). This morphological evolution follows the principles of Ostwald ripening, where initial small clusters dissolve, promoting the growth of polycrystals driven by the Gibbs-Thomson effect.[37] FTIR spectra of Py-1P formed at different times confirmed consistent imine linkages with minimal variation (Supplementary Fig. 24). It suggests self-correction guided by dynamic covalent chemistry within Py-1P frameworks,[38] which could eliminate initial defects to yield better crystallized frameworks. Accordingly, time-resolved PXRD patterns showed increasingly intense diffraction peaks with extended synthesis time (Fig. 1e). The reduction in framework defects in turn promoted porosity and pore volume (Fig. 1f and Supplementary Fig. 25). Py-1P-6-72 demonstrated a notable Brunauer-Emmett-Teller (BET) surface area of 2880 $m^2\ g^{-1}$ and a pore volume of 1.51 $cm^3\ g^{-1}$. This substantial porosity enabled efficient vapor sorption across a range of solvents (Fig. 1g and Supplementary Fig. 26).

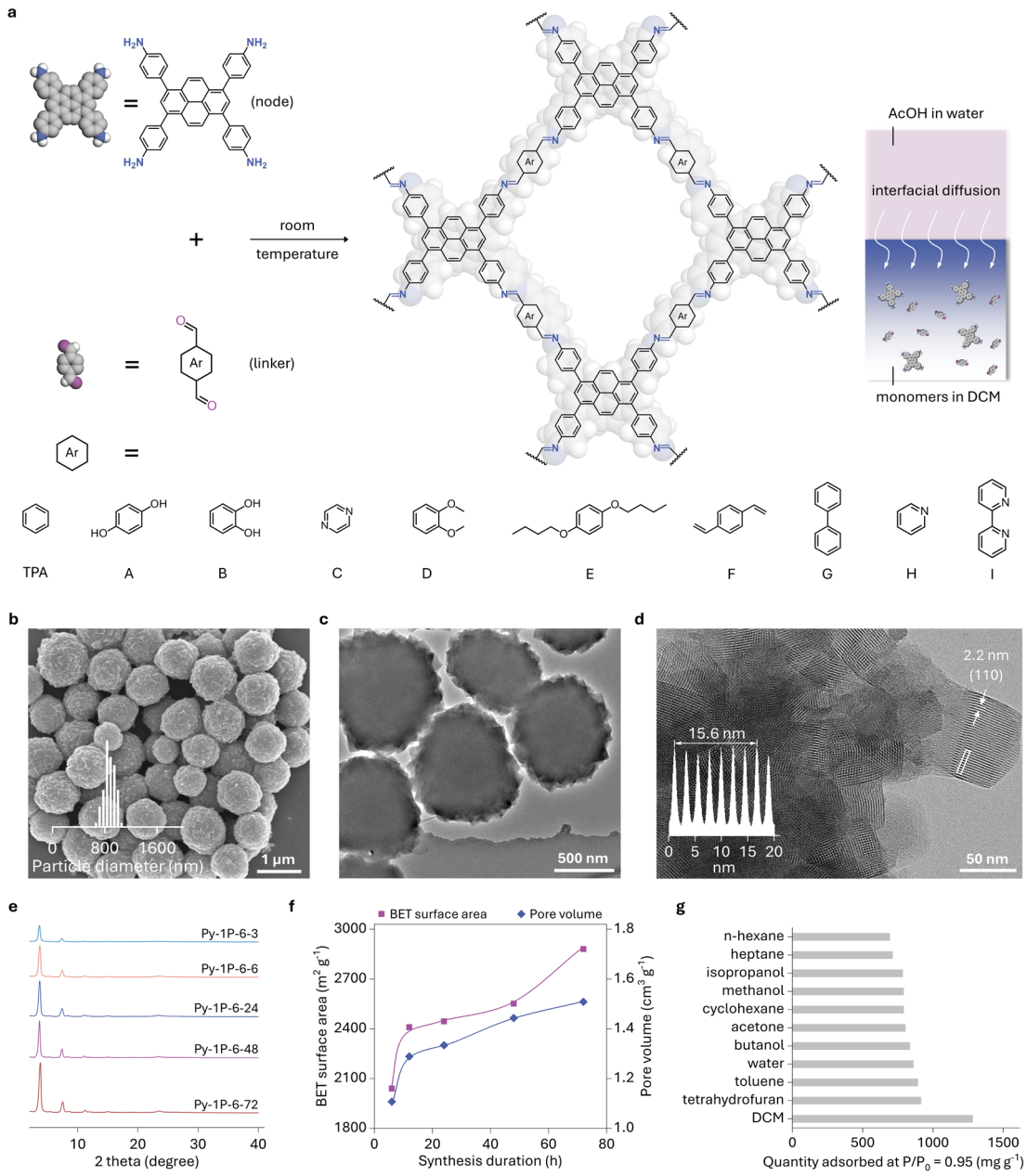

Fig. 1. Synthesis and characterization of Py-COF polycrystals. a, Schematic illustration of the chemical structures and condensation reaction between $Py(NH_2)_4$ node and dialdehyde linkers. **b**, SEM image of Py-1P-6-72. The inset shows its diameter distribution. **c**, TEM image of Py-1P-6-72. **d**, HRTEM image of Py-1P-6-72. The inset shows the line profile along the boxed region, giving the spacing of (110) planes. **e**, PXRD patterns of Py-1P-6-b. **f**, BET surface areas and pore volumes of Py-1P-6-b. **g**, Vapor sorption quantities of Py-1P-6-72.

Catalyst acidity potentially affects the crystallinity and morphology of Schiff-base COFs.[39] To investigate this, we performed structural analyses of Py-1P-a-72 samples. Although their FTIR spectra were comparable (Supplementary Fig. 27), PXRD patterns showed evident differences in crystallinity (Fig. 2a). The use of water-diluted AcOH produced highly crystalline Py-1P even at molarities as high as 15 M, whereas the use of glacial AcOH resulted in poorly crystallized frameworks (Supplementary Fig. 28). This contrast aligns with the biphasic system design, where the created interface slows AcOH diffusion, thus retarding condensation and promoting crystallization.[32] Optimal crystallinity was achieved at 6 M AcOH. SEM images further revealed visible morphological variations as AcOH molarity increased from 3 M to glacial (Fig. 2b and Supplementary Fig. 29). At 6 M AcOH, Py-1P-6-72 exhibited tightly packed polyhedral crystals aggregated into spherical structures. In contrast, higher acidity appeared to protonate the imine linkages, generating electrostatic repulsion that led to polyhedral separation. Moreover, the use of glacial AcOH resulted in a complete loss of polyhedral textures and the formation of small, irregular particles, implying a significant decline in crystallinity. 77 K N_2 sorption results manifested changes in Py-1P microporosity across different AcOH molarities (Fig. 2c and Supplementary Fig. 30). Notably, the variations in pore volume did not fully agree with the changes in BET surface area. This implies that inappropriate acidity could hinder monomer condensation, thus producing framework defects. This was corroborated by the hysteresis loop in the desorption isotherm of Py-1P-glacial-72. Pore size distributions obtained from density functional theory fitting revealed the presence of obvious pore defects larger than 3 nm in Py-1P-3-72 and Py-1P-glacial-72 (Fig. 2d). Furthermore, the ^{1}H NMR spectrum determined a nearly perfect structure of Py-1P-6-72, with a monomer ratio closely matching the theoretical value of 0.5 (Fig. 2e). Near-edge X-ray absorption fine structure (NEXAFS) spectroscopy offered additional confirmation, showing a higher proportion of imine linkages in Py-1P-6-72 compared to Py-1P-3-72 and Py-1P-glacial-72 (Fig. 2f).[40] These findings show

the control over Py-1P structure by altering catalyst acidity.

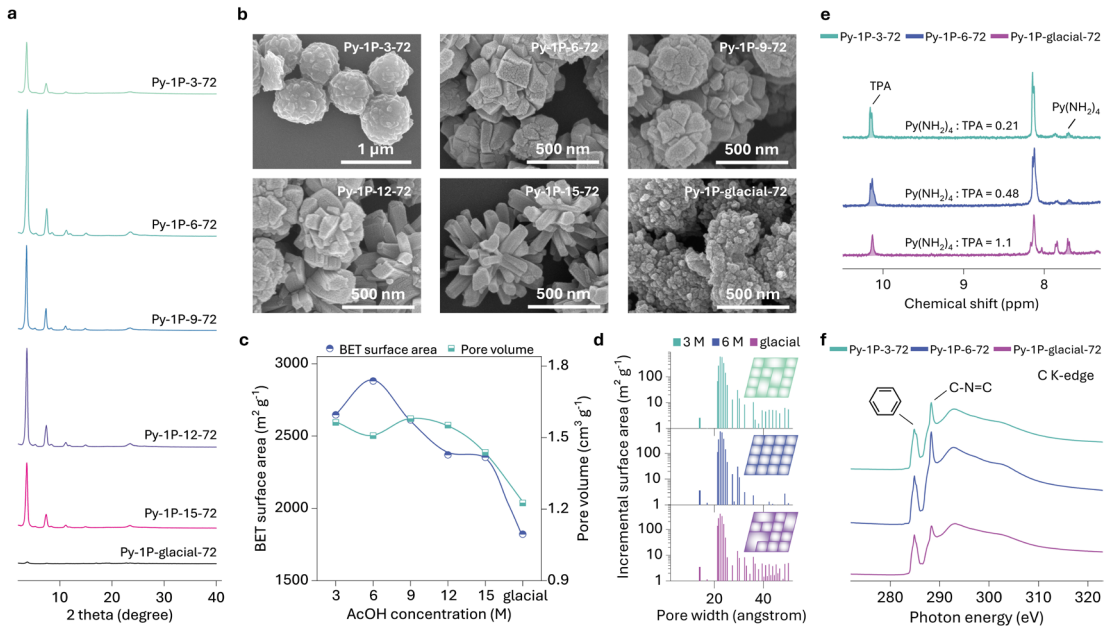

Fig. 2. Characterization of Py-1P-a-72. a, PXRD patterns. **b**, SEM images. **c**, BET surface areas and pore volumes. **d**, Pore size distributions, **e**, ^{1}H NMR spectra, and **f**, C K-edge NEXAFS spectra of Py-1P-3-72, Py-1P-6-72, and Py-1P-glacial-72.

Py-1P polyhedral crystal films

The growth of Py-1P polycrystals motivated us to develop polyhedral crystal films under ambient conditions (Supplementary Fig. 31). To enrich active growth sites, we pretreated the glass synthesis bottle with an alkaline bath, enabling crystal growth on the bottle walls to produce films. This growth process follows a solid-liquid interfacial methodology,[41] allowing for confined crystal growth on solid substrates to give polyhedral films while forming polycrystals in DCM simultaneously. The resulting film could be transferred onto a plastic ring (Supplementary Fig. 32), showing physical flexibility in contrast to the rigidity of MOF analogues.[42] Using a silicon wafer as the substrate, we produced continuous crystal-intergrown films featuring a prominent polyhedral texture (Fig. 3a and Supplementary Fig. 33). Spectroscopic analyses, including FTIR, Raman, ^{13}C NMR, and X-ray photoelectron spectroscopy (XPS), confirmed the formation of Py-1P films rather than monomer recrystallization (Supplementary

Figs. 34-37). This marks the advent of COF crystal thin films with an unusual polyhedral texture reminiscent of MOF analogues. The polyhedral texture starkly contrasts with the indistinctive surfaces of reported COF films,[31] including routine Py-1P films.[43,44] Unlike relatively thick MOF counterparts,[18] this COF polyhedral film gave a uniform and nanoscale thickness of ~360 nm (Fig. 3b and Supplementary Fig. 38). By lowering the monomer concentration, we thinned Py-1P polyhedral films to thicknesses as low as 140 nm while preserving high crystal quality and sharp diffractions (Supplementary Fig. 39). Moreover, the ambient conditions here distinguish our organic crystal film fabrication from the harsh environments required for inorganic crystal film growth,[45] making it suitable for industrial manufacturing.

Notably, the PXRD pattern of Py-1P-6-72 polyhedral film substantially replicated that of polycrystals (Supplementary Fig. 40). Low-dose HRTEM images revealed interlaced lattice fringes with diffraction signals from the (110), (200), (220), (330), and (440) planes in the fast Fourier transform (FFT) image (Fig. 3c and Supplementary Fig. 41). These high-index crystal facets validate the long-range order of our polyhedral film. Pawley refinement of its experimental PXRD pattern yielded unit cell parameters of a = 21.64 Å, b = 22.54 Å, c = 3.69 Å, α = 87.84°, β = 87.71°, and γ = 85.68°, with R_p = 4.77% and R_{wp} = 6.33% (Supplementary Fig. 42). Grazing-incidence wide-angle X-ray scattering (GIWAXS) results confirmed the polycrystalline nature of this Py-1P-6-72 film, showing powder rings with diffraction projection signals at q = 2.9 and 5.7 nm^{-1} from the (110) and (220) planes, respectively (Supplementary Fig. 43). The Py-1P-6-72 film exhibited high crystallinity and consistent crystal textures across 12 replicates, with a narrow and symmetric distribution of the (110) full width at half maximum (FWHM) (Fig. 3d and Supplementary Fig. 44), showing high reproducibility. Our method also proved excellent adaptability across a wide range of substrates, including glass plates, porous polymer membranes, and alumina disks (Supplementary Figs. 45-47). The Py-1P-6-72 film grown on an alumina disk exhibited PXRD peak intensities comparable to a

polycrystalline MOF (termed UiO-66) membrane (Supplementary Fig. 47), highlighting its remarkable crystallinity. When grown on porous polymer substrates (Supplementary Fig. 46), these polyhedral membranes hold potential for separation applications, which are currently under exploration.

Time-resolved PXRD tracked the growth of Py-1P films on a silicon wafer (Fig. 3e). After 6 h, Py-1P diffraction peaks were undetected, although SEM images showed a continuous film with scattered grain-like crystal nuclei (Supplementary Fig. 48a). At 24 h, Py-1P diffraction peaks emerged with an incipient polyhedral texture, which became more pronounced at 48 and 72 h (Supplementary Fig. 48b-d). Atomic force microscopy (AFM) showed an increase in the film's root mean square roughness (R_q) from 10.1 to 19.4 nm (Supplementary Fig. 49), along with concurrent growth in both crystal size and film thickness (Supplementary Fig. 50). This crystal growth correlates with a reduction in FWHM values for the primary diffraction peak at 3.7° (Supplementary Fig. 51). The FWHM value decreased from 0.736° at 36 h to 0.426° at 48 h, and then stabilized at 0.412° after 72 h, suggesting that crystallization was almost complete by 48 h.[46] With a synthesis time of 72 h, the AcOH molarity was optimized to be 6 M to deliver strikingly polyhedral films (Supplementary Figs. 52-53). Significantly, we achieved uniform 4-inch wafer-scale Py-1P-6-72 polyhedral films (Fig. 3f, g and Supplementary Fig. 54), showing the scalability of our approach.

N_2 sorption experiments at 77 K revealed impressive BET surface areas of 1777 and 2101 $m^2 g^{-1}$ for Py-1P-6-48 and Py-1P-6-72 films, respectively (Fig. 3h and Supplementary Fig. 55). Their pore widths were centered around 2.2 nm, consistent with that of the theoretical model. Comparative analyses placed the BET surface area of Py-1P-6-72 among the top three reported COF films, with values 2-80 times higher than COF films of similar pore sizes (1.8-2.5 nm) (Fig. 3i and Supplementary Table 1). This substantial BET surface area is a result of the well-organized and accessible pore structures within the polyhedral film. The Py-1P-6-72 crystal film demonstrated outstanding chemical stability. It

retained its surface morphology, weight, microporosity, and crystallinity even after prolonged exposure to harsh conditions, including 6 months in air and various solvents, 3 days in boiling water, and 24 h in 6 M NaOH and HCl solutions (Fig. 3j and Supplementary Figs. 56-58). This robustness highlights the potential of Py-1P polyhedral crystal films for practical applications.

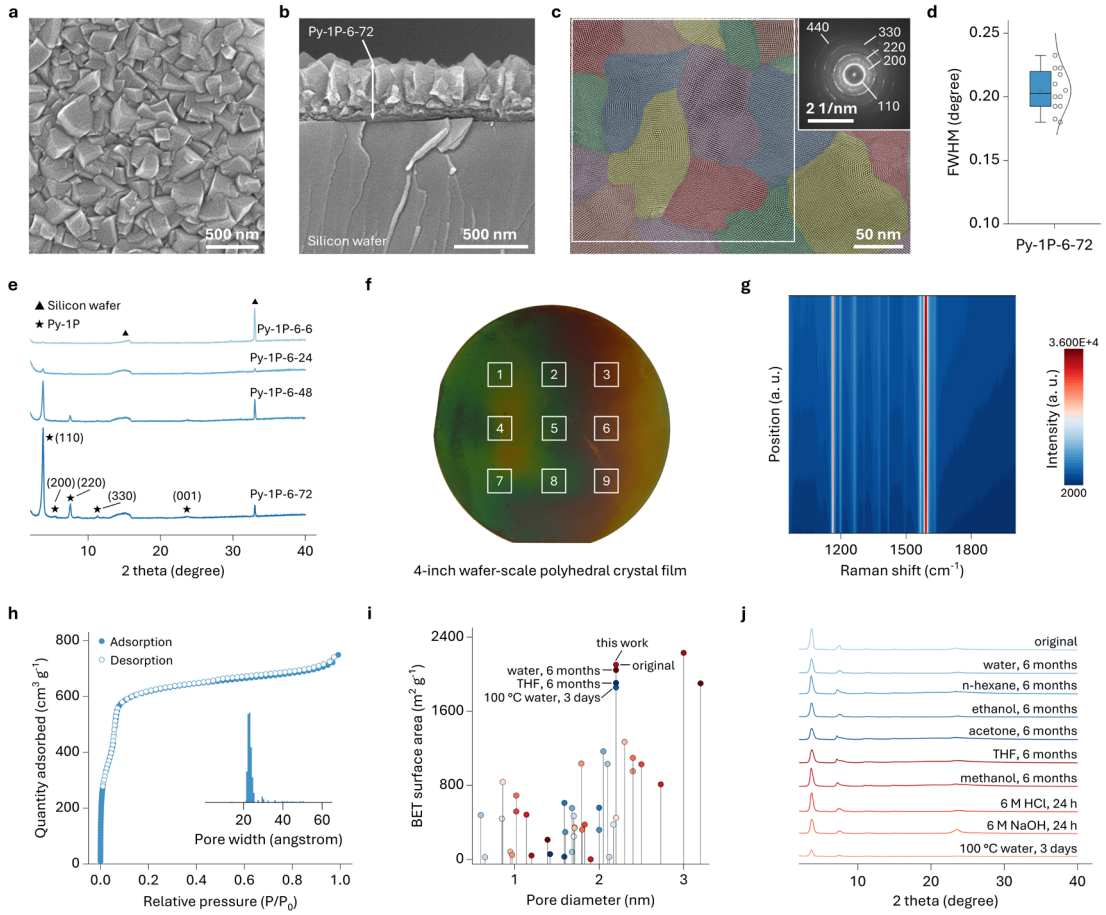

Fig. 3. Py-1P polyhedral crystal films. a, Surface and **b**, cross-sectional SEM images of the Py-1P-6-72 film. **c**, False-colored HRTEM image of the Py-1P-6-48 film. The inset shows FFT of the boxed region. **d**, Box-and-whisker plots of FWHM values for the Py-1P-6-72 films across 12 replicates. **e**, PXRD patterns of the Py-1P-6-b films. A piece of film grown on a silicon wafer was used for the PXRD test. **f**, Photograph of a 4-inch wafer-scale Py-1P-6-72 film. **g**, Raman spectral contour map of the 4-inch Py-1P-6-72 film with data collected across 9 areas in (**e**). **h**, 77 K N_2 adsorption-desorption isotherms of the Py-1P-6-72 film. The inset shows the pore size distribution. **i**, BET surface area comparison

between the reported COF films and Py-1P-6-72 film. Detailed information is provided in Supplementary Table 1. **j**, PXRD patterns of the Py-1P-6-72 film subjected to various treatments.

Real-space insights into polyhedral crystal film growth

To gain structural insights beyond the analyses by diffraction and sorption techniques, time-dependent Py-1P films were grown on an 8-nm-thick amorphous silicon dioxide film supported by a silicon nitride mesh TEM grid, followed by low-dose HRTEM analysis (Fig. 4a). Optical and TEM images revealed the morphological features of Py-1P-6-6 directly grown on the silicon grid during initial growth, avoiding interference from film transfer (Fig. 4b and Supplementary Fig. 59). After 1.5-h growth, the Py-1P crystal nuclei were clearly visible under TEM, with the in-plane size ranging from 20 to 80 nm (Fig. 4c and Supplementary Fig. 60). These nuclei exist in both crystalline and amorphous phases, highlighted by white- and black-boxed areas, respectively. Grain boundaries, marked by white lines, indicated the merging of nuclei from different crystallographic directions (Fig. 4c, d). The well-crystallized regions, characterized by distinct lattice fringes, expanded from 20-40 nm at 1.5 h to 40-70 nm at 3 h (Supplementary Fig. 61), suggesting nucleation-elongation processes that could occur at similar timescales.[47,48] After 6 h, multilayered crystals were formed, resulting in a continuous film (Fig. 4e). Extending the growth period to 72 h facilitated further crystallization and connectivity of crystals, yielding a fully continuous Py-1P polyhedral film with interlaced lattice fringes across HRTEM images (Fig. 4f and Supplementary Fig. 62). High-index plane diffraction spots also emerged in the corresponding FFT (Supplementary Fig. 63). For out-of-plane growth, we captured interlayer slipping in the early stage of nucleation. Instead of the expected eclipsed AA stacking, we observed ectopic AB stacking of Py-1P layers,[49,50] with a slipping distance of 1.1 nm (Supplementary Fig. 64a-b). Pronounced slipping in an ABC stacking mode, with slipping distances of 0.65 and 1.26 nm, was also visualized

(Supplementary Fig. 64c-d). These suggest local misalignment between adjacent Py-1P nuclei during vertical expansion.

To further resolve real-space structures of early-stage crystal nuclei, integrated differential phase contrast scanning transmission electron microscopy (iDPC-STEM) was employed.[51] Imaging the nuclei after 1.5-h growth revealed predominant crystal growth along the [001] and slightly tilted [001] crystallographic directions (Fig. 4g and Supplementary Fig. 65). High-angle annular dark-field (HAADF) STEM images further confirmed the atomic ordered arrangement projection (Fig. 4h). Some nuclei exhibited unique crystal bending (Fig. 4i, j, and Supplementary Fig. 66), probably caused by directional changes of the imine bonds.[52] We also observed topological isomerism in the nuclei, suggesting polymorphism within Py-1P polyhedral films. The topology is dominated by quasi-square lattice (sql), together with a minor fraction of kagome (kgm) topology (Fig. 4k and Supplementary Fig. 67). Triangular and hexagonal pores were identified in the kgm topology, while quadrangular pores were observed in the sql topology. The lattice parameters of the sql-topology Py-1P were measured as $a = b = 2.44 \pm 0.1$ nm; $\gamma = 85 \pm 1°$, consistent with a heterodromous motif of imine bonds.[52] These findings reveal that COF crystal films exhibit significantly more complex structures compared to previously assumed simplistic models.[53]

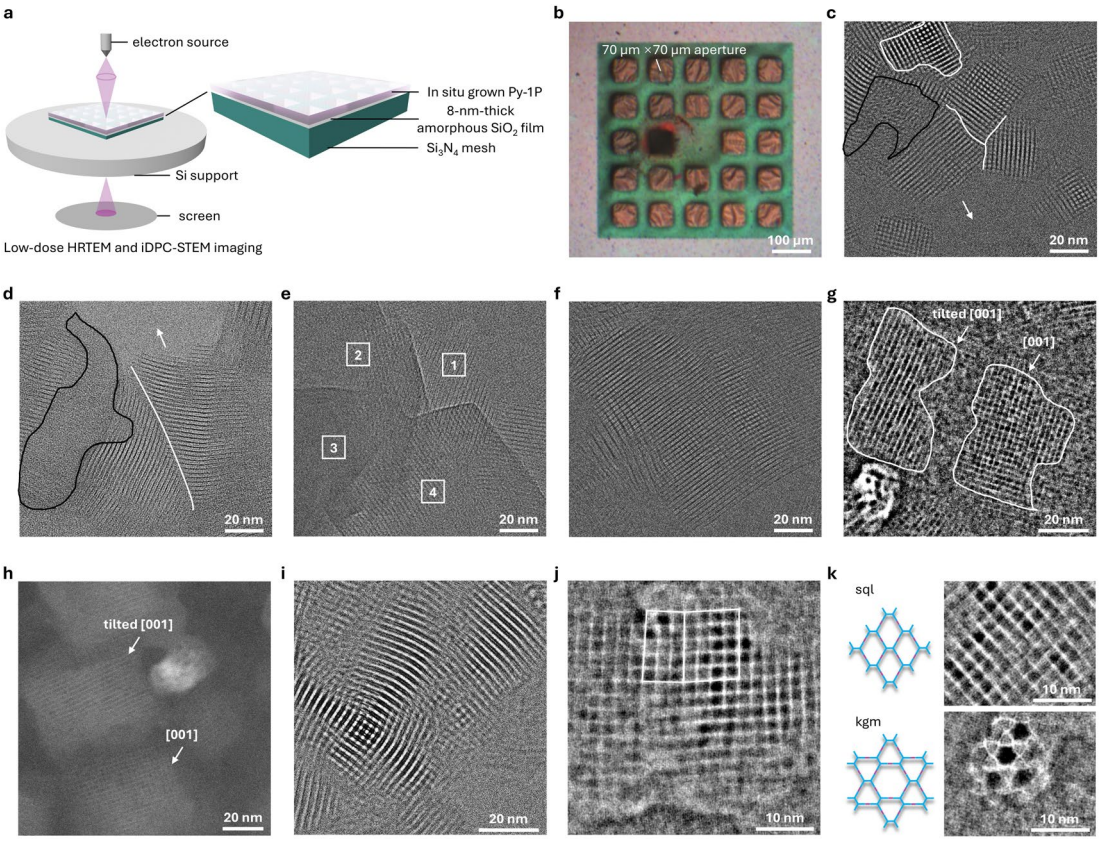

Fig. 4. Real-space insights into Py-1P polyhedral crystal film growth. a, Schematic illustration for low-dose HRTEM analysis of Py-1P directly grown on a silicon-based TEM grid. **b**, Optical image of Py-1P-6-6 grown on the TEM grid. **c-f**, Low-dose HRTEM images of Py-1P-6-1.5, Py-1P-6-3, Py-1P-6-6, and Py-1P-6-72. **g**, iDPC-STEM and **h**, HAADF-STEM images of Py-1P-6-1.5. **i**, Low-dose HRTEM and **j**, iDPC-STEM images showing the crystal bending of Py-1P-6-1.5. **k**, Low-dose HRTEM (above) and iDPC-STEM (below) images showing the polymorphism of Py-1P-6-1.5.

Methodological universality

We expanded our method to produce various Py-COF polyhedral crystal films by covalently linking $Py(NH_2)_4$ with diverse dialdehydes under the optimal conditions used for Py-1P. SEM and AFM analyses revealed the polyhedral textures of these films with R_q values of ~17-52 nm (Fig. 5a, b). These films are thin, with thicknesses measured at 200, 210, 240, 650, and 470 nm for Py-D, Py-E, Py-F, Py-G, and Py-I, respectively, matching AFM height profiles (insets

in Fig. 5a and Supplementary Figs. 68-70). These films showed high crystallinity, as evidenced by sharp diffraction peaks from the (110) and (220) planes (Fig. 5c). Diffraction peaks around 24°, associated with the (001) plane, revealed their two-dimensionally layered structures (insets in Fig. 5c). N_2 sorption tests at 77 K determined ample microporosities of Py-COF polyhedral films (Supplementary Fig. 71). This approach further led to COF polycrystalline heterostructures. Using TPA and 4,4''-*p*-terphenyldicarboxaldehyde (J) as linkers, we fabricated a Py-J-on-Py-1P polycrystalline heterostructure (Fig. 5d). Cross-sectional SEM imaging confirmed its composite nature (Fig. 5e and Supplementary Fig. 72). The PXRD pattern showed prominent diffraction peaks from both Py-1P and Py-J, confirming its highly crystalline feature (Fig. 5f). With a dual-layer functional design, such COF polycrystalline heterostructures offer promise for catalysis, energy storage, and beyond.[54,55]

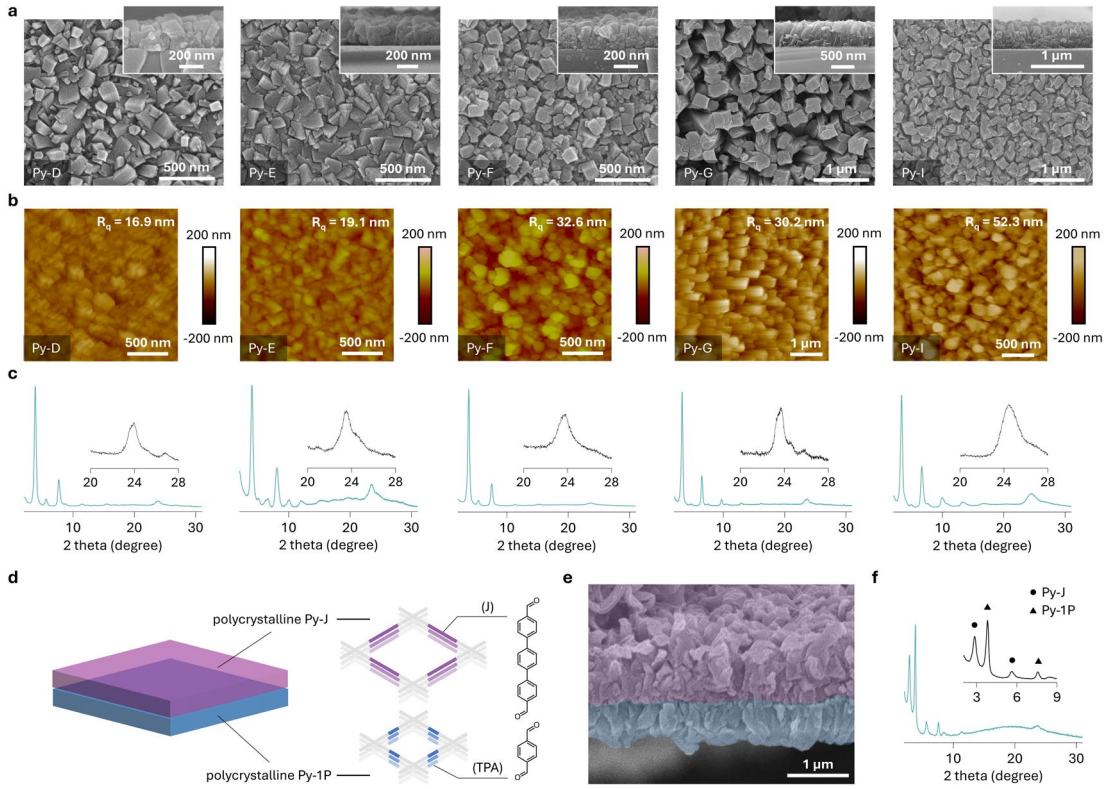

Fig. 5. Py-COF polyhedral crystal films and heterostructures. a, SEM images of the Py-COF films grown on silicon wafers. Insets show their cross-sectional SEM images. **b**, AFM images of the Py-COF films. **c**, PXRD patterns

of the Py-COF films. Insets show the PXRD patterns with a 2-theta range of 20-28°. **d**, Schematic illustration of a Py-J-on-Py-1P heterostructure. **e**, False-colored cross-sectional SEM image of the Py-J-on-Py-1P heterostructure. **f**, PXRD pattern of the Py-J-on-Py-1P heterostructure. The inset shows the PXRD pattern with a 2-theta range of 2-9°.

Thermal flexibility of Py-COF polyhedral crystal films

While COF flexibility toward guest molecules such as gases and solvents has been reported,[56-58] the exploration of their thermal flexibility, especially in COF polyhedral films, remains limited. To address this gap, we investigated the thermal flexibility of Py-COF polyhedral films using variable-temperature PXRD measurements. Polyhedral films grown on silicon wafers were mounted on a thermal specimen stage equipped with a precise thermocouple for controlled heating and cooling (Fig. 6a). Measurements were conducted under both atmospheric conditions and inert environments with N_2 purging. In N_2, the diffraction peaks corresponding to the (110) and (220) planes of Py-1P-6-72 at 3.7° and 7.5°, respectively, remained stable up to 350 °C (Fig. 6b), indicating high thermal stability, which agrees with the result of thermogravimetric analysis (Supplementary Fig. 73). However, the (001) plane diffraction, associated with the π-π stacking of Py-1P, shifted continuously toward lower 2-theta positions as the temperature increased from 50 to 350 °C (Fig. 6c). Upon cooling, the diffraction peak reverted to its original position, indicating thermally flexible structural dynamics. Similar phenomena were observed under atmospheric conditions (Supplementary Fig. 74). The distinct responses of the (110) and (001) planes suggest anisotropic thermal expansion, likely due to the strong in-plane covalent bonds and weaker out-of-plane π-π interactions in Py-1P. Using Bragg's law, the interlayer spacing was quantified as a function of temperature. At 50 °C, the interlayer spacing of Py-1P-6-72 was 3.76 Å, which expanded to 3.99 Å at 350 °C (Fig. 6d). This positive and linear thermal expansion yields a thermal expansion coefficient (TEC) of 1.96×10^{-4} K^{-1}, exceeding those of

inorganic materials.[59]

This thermal flexibility is consistent across Py-COF polyhedral films with different dialdehyde linkers. They demonstrated high thermal stability, with minimal changes in the intensity of the diffraction peaks from the (110) and (220) planes at elevated temperatures (Supplementary Figs. 75-78). Their interlayer distances exhibited similar positive and linear temperature-dependent variations. Notably, the TECs of polyhedral films follow the order of Py-G > Py-1P > Py-C > Py-I ≈ Py-D, with respective values of 2.15, 1.96, 1.73, 1.65, and 1.64 × 10^{-4} K^{-1} (Fig. 6e). This trend reflects the influence of electron-donating substituents on the benzene rings of the dialdehyde linkers, which reinforce interlayer interactions to resist thermal expansion.[59,60] In situ variable-temperature FTIR results elucidated reversible structural deformations, revealing temperature-induced dynamic shifts in the stretching vibrations of aromatic backbones in Py-1P (Fig. 6f). Comparatively weaker shifts were observed for Py-I, consistent with improved interlayer interactions that limit thermal flexibility relative to Py-1P and Py-G (Supplementary Fig. 79). We next examined the temperature-dependent changes in film thickness and surface roughness using in situ variable-temperature spectroscopic ellipsometry (Fig. 6g). The film thickness increased from 149 nm at 50 °C to 157.4 nm at 250 °C, then reverted to 149.2 nm upon cooling to 50 °C (Fig. 6h). Throughout this process, the film surface roughness remained consistent, indicating that the thickness variations arise from interlayer expansion instead of morphological changes. Moreover, the two short-term thickness fluctuations observed during heating and cooling captured the dynamic expansion and contraction of Py-1P layers. The experimentally measured thickness increment of 8.4 nm closely matches the value of 6.2 nm estimated through PXRD data, confirming the crystallographic thermal flexibility of Py-COF polyhedral films.

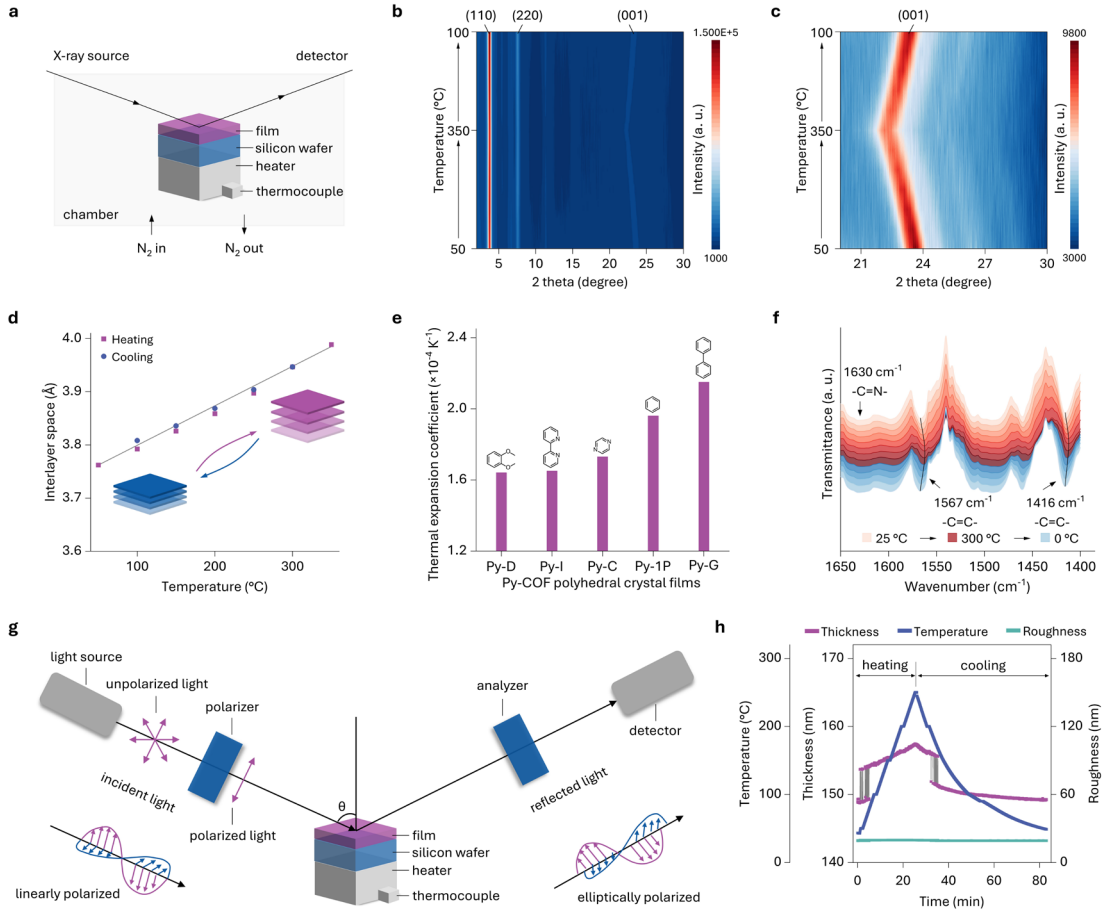

Fig. 6. Thermal flexibility of Py-COF polyhedral crystal films. a, Schematic illustration of the variable-temperature PXRD test. **b**, Contour map of the variable-temperature PXRD patterns of the Py-1P-6-72 polyhedral film in N_2. **c**, Contour map of the variable-temperature PXRD patterns of the Py-1P-6-72 polyhedral film in N_2. **d**, Temperature-dependent interlayer spaces of the Py-1P-6-72 polyhedral film. **e**, Thermal expansion coefficients of the Py-COF polyhedral films. **f**, In situ variable-temperature FTIR spectra of the Py-1P-6-72 polycrystal. **g**, Schematic illustration of spectroscopic ellipsometry. **h**, Temperature-dependent thickness and roughness changes of the Py-1P-6-72 polyhedral film. The polyhedral film in (**h**) was synthesized using 0.35 times the original monomer concentration.

Film crystallinity-performance correlation

Next, the interplay between film crystallinity and device performance was investigated using a sensor platform. By varying synthesis time and AcOH

molarity, Py-1P films with different degrees of crystallinity were in situ grown on interdigitated electrodes to produce sensor devices (Fig. 7a). Optical microscopy, SEM, and energy dispersive X-ray spectrometry verified the uniform growth of polyhedral films across the electrode surface (Fig. 7b and Supplementary Figs. 80-81). Current signals of these sensor devices were monitored at room temperature under exposure to gaseous analytes through an integrated sensor system (Supplementary Fig. 82). Current-voltage curves revealed increased conductivity at elevated temperatures (Fig. 7c and Supplementary Fig. 83), indicative of the semiconducting characteristic of the films. These sensors demonstrated high sensitivity to nitrogen dioxide (NO_2), detecting concentrations as low as 1 ppm. Among the Py-1P-a-72 films, the Py-1P-6-72 film showed the highest response values across NO_2 concentrations of 1, 2, 3, and 5 ppm, with respective values of 2.5, 8.4, 32.2, and 153.4 (Fig. 7d). Prolonging synthesis time at 6 M AcOH also enhanced NO_2 sensing performance (Fig. 7e). These results establish a positive correlation between film crystallinity and device sensitivity.

To explore the effect of crystallinity on sensor selectivity, we exposed these films to various interfering gases, including toluene, hydrogen sulfide (H_2S), acetone, and ammonia (NH_3) (Supplementary Fig. 84). The polyhedral films showed superior selectivity toward NO_2 (Fig. 7f), mainly due to the strong affinity between imine linkages and NO_2 molecules.[61] Among the tested films, the Py-1P-6-72 film exhibited the highest selectivity (Fig. 7g), with an NO_2 response about 53 times higher than that for toluene, emphasizing the critical role of crystallinity in specific recognition of sensors. Beyond sensitivity and selectivity, the Py-1P-6-72 film sensor also demonstrated remarkable durability with its response uncompromised over 150 days (Fig. 7h and Supplementary Fig. 85). Compared to metal-based porous materials, this pure-organic Py-1P polyhedral film exhibited superior ppm-level NO_2 detection at room temperature (Supplementary Table 2). Moreover, a microcantilever sensor was also developed for effectively monitoring NO_2 (Fig. 7i), showcasing the potential for

compact, portable, and wearable devices.

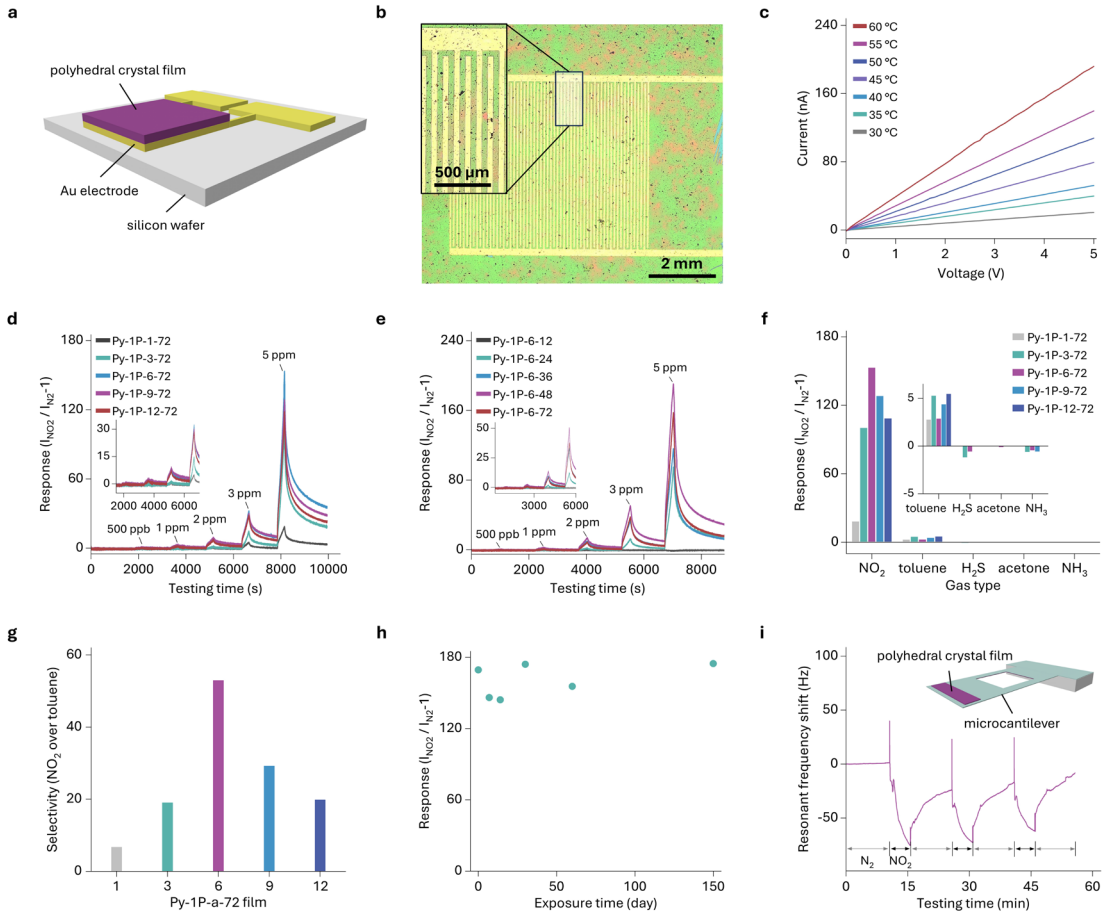

Fig. 7. Film crystallinity and sensor performance correlation. a, Schematic illustration of sensor devices. **b**, Optical microscopy image of the sensor device with a Py-1P-6-24 film. The inset shows the enlarged image. **c**, Current-voltage curves of the sensor with a Py-1P-6-72 film at various temperatures. **d**, NO_2 responses of the sensors with Py-1P-a-72 films. **e**, NO_2 responses of the sensors with Py-1P-6-b films. Insets in (**d**) and (**e**) show the responses to low-concentration NO_2. **f**, Gas responses of the sensors with Py-1P-a-72 films. The inset shows the responses toward interfering gases. **g**, Selectivity of the sensors with Py-1P-a-72 films. **h**, NO_2 responses of the Py-1P-6-72 sensor film after exposure to air. **i**, Resonant frequency change of the Py-1P-6-72 microcantilever sensor. The inset shows its schematic illustration.

Discussion

We have synthesized a series of robust Py-COF polycrystals and polyhedral

crystal films using a scalable biphasic approach under ambient conditions. These films demonstrated prominent structural order and polyhedral textures, comparable to those observed in MOF counterparts. Our method is not only reproducible but also highly adaptable for manufacturing large-size polyhedral films on various substrates toward industrial production. Particularly, the Py-1P polyhedral film achieved exceptional crystallinity, chemical stability, and microporosity, with the highest BET surface area reported for COF films with similar pore sizes. Synergistic imaging using low-dose HRTEM and iDPC-STEM determined previously ambiguous crystallographic slipping, bending, and topological isomerism in the Py-1P crystal film. We further elucidated the anisotropic thermal flexibility of polyhedral films along the [001] crystal direction, characterized by dynamically adaptive thermal expansion with TECs estimated at 1.64-2.15 × 10^{-4} K^{-1}. Using a sensor platform, we demonstrated that enhanced crystallinity in Py-1P crystal films significantly improves device performance. Our findings challenge the prevailing consensus that COF films are flat and non-textured owing to their polymer-like characteristics. By leveraging their polymer and, more importantly, crystal nature, we show a facile pathway to high-quality COF polyhedral crystal films with excellent mechanical flexibility. This work heralds the advent of polyhedral COF films and will unlock vast opportunities for their industrialization and application across diverse fields.

References

1. Côté, A. P. *et al.* Porous, crystalline, covalent organic frameworks. *Science* **310**, 1166-1170 (2005).

2. Horike, S., Shimomura, S. & Kitagawa, S. Soft porous crystals. *Nat. Chem.* **1**, 695-704 (2009).

3. Yazyev, O. V. & Chen, Y. P. Polycrystalline graphene and other two-dimensional materials. *Nat. Nanotechnol.* **9**, 755-767 (2014).

4. Gu, H. *et al.* Phase-pure two-dimensional layered perovskite thin films. *Nat. Rev. Mater.* **8**, 533-551 (2023).

5. Jiang, H., Alezi, D. & Eddaoudi, M. A reticular chemistry guide for the design of periodic solids. *Nat. Rev. Mater.* **6**, 466-487 (2021).

6. Li, H. *et al.* Na^+-gated water-conducting nanochannels for boosting CO_2 conversion to liquid fuels. *Science* **367**, 667-671 (2020).

7. Zhou, Z. *et al.* Carbon dioxide capture from open air using covalent organic frameworks. *Nature* **635**, 96-101 (2024).

8. Furukawa, H., Cordova, K. E., O'Keeffe, M. & Yaghi, O. M. The chemistry and applications of metal-organic frameworks. *Science* **341**, 1230444 (2013).

9. Koner, K. *et al.* Porous covalent organic nanotubes and their assembly in loops and toroids. *Nat. Chem.* **14**, 507-514 (2022).

10. Xu, Y. *et al.* Symmetry-breaking dynamics in a tautomeric 3D covalent organic framework. *Nat. Commun.* **14**, 4215 (2023).

11. Freund, R. *et al.* The current status of MOF and COF applications. *Angew. Chem., Int. Ed.* **60**, 23975-24001 (2021).

12. Yin, Y. *et al.* Ultrahigh-surface area covalent organic frameworks for methane adsorption. *Science* **386**, 693-696 (2024).

13. Zheng, L. *et al.* Covalent organic framework membrane reactor for boosting catalytic performance. *Nat. Commun.* **15**, 6837 (2024).

14. Zhou, S. *et al.* Asymmetric pore windows in MOF membranes for natural gas valorization. *Nature* **606**, 706-712 (2022).

15. Fu, J. *et al.* Fabrication of COF-MOF composite membranes and their highly selective separation of H_2/CO_2. *J. Am. Chem. Soc.* **138**, 7673-7680 (2016).

16. Shi, X. *et al.* Selective liquid-phase molecular sieving via thin metal-organic framework membranes with topological defects. *Nat. Chem. Eng.* **1**, 483-493 (2024).

17. Zhao, S. *et al.* Hydrophilicity gradient in covalent organic frameworks for membrane distillation. *Nat. Mater.* **20**, 1551-1558 (2021).

18. Knebel, A. & Caro, J. Metal-organic frameworks and covalent organic frameworks as disruptive membrane materials for energy-efficient gas separation. *Nat. Nanotechnol.* **17**, 911-923 (2022).

19. Denny, M. S., Moreton, J. C., Benz, L. & Cohen, S. M. Metal-organic frameworks for membrane-based separations. *Nat. Rev. Mater.* **1**, 16078 (2016).

20. Burke, D. W., Jiang, Z., Livingston, A. G. & Dichtel, W. R. Two-dimensional covalent organic framework membranes for liquid-phase molecular separations: state of the field, common pitfalls, and future opportunities. *Adv. Mater.* **36**, 2300525 (2024).

21. Yang, Y. *et al.* Elastic films of single-crystal two-dimensional covalent organic frameworks. *Nature* **630**, 878-883 (2024).

22. Ma, T. *et al.* Single-crystal x-ray diffraction structures of covalent organic frameworks. *Science* **361**, 48-52 (2018).

23. Han, J. *et al.* Fast growth of single-crystal covalent organic frameworks for laboratory x-ray diffraction. *Science* **383**, 1014-1019 (2024).

24. Evans, A. M. *et al.* Seeded growth of single-crystal two-dimensional covalent organic frameworks. *Science* **361**, 52-57 (2018).

25. Kandambeth, S. *et al.* Selective molecular sieving in self-standing porous covalent-organic-framework membranes. *Adv. Mater.* **29**, 1603945 (2017).

26. Yin, C. *et al.* Perpendicular alignment of covalent organic framework (COF) pore channels by solvent vapor annealing. *J. Am. Chem. Soc.* **145**, 11431-11439 (2023).

27. Li, Y. *et al.* Laminated self-standing covalent organic framework membrane with uniformly distributed subnanopores for ionic and molecular sieving. *Nat. Commun.* **11**, 599 (2020).

28. Yuan, J. *et al.* Photo-tailored heterocrystalline covalent organic framework membranes for organics separation. *Nat. Commun.* **13**, 3826 (2022).

29. Cao, L. *et al.* Switchable Na^+ and K^+ selectivity in an amino acid functionalized 2D covalent organic framework membrane. *Nat. Commun.* **13**, 7894 (2022).

30. Wang, M. *et al.* Ultrafast seawater desalination with covalent organic framework membranes. *Nat. Sustain.* **5**, 518-526 (2022).

31. Shi, X. *et al.* Design of three-dimensional covalent organic framework membranes for fast and robust organic solvent nanofiltration. *Angew. Chem., Int. Ed.* **61**, e202207559 (2022).

32. Liu, J. *et al.* Self-standing and flexible covalent organic framework (COF) membranes for molecular separation. *Sci. Adv.* **6**, eabb1110 (2020).

33. Fan, H. W. *et al.* High-flux vertically aligned 2D covalent organic framework membrane with enhanced hydrogen separation. *J. Am. Chem. Soc.* **142**, 6872-6877 (2020).

34. Fenton, J. L., Burke, D. W., Qian, D., Olvera de la Cruz, M. & Dichtel, W. R. Polycrystalline covalent organic framework films act as adsorbents, not membranes. *J. Am. Chem. Soc.* **143**, 1466-1473 (2021).

35. Shi, X. *et al.* Precise separation of complex ultrafine molecules through solvating two-dimensional covalent organic framework membranes. *Angew. Chem., Int. Ed.* **64**, e202421661 (2025).

36. Auras, F. *et al.* Synchronized offset stacking: a concept for growing large-domain and highly crystalline 2D covalent organic frameworks. *J. Am. Chem. Soc.* **138**, 16703-16710 (2016).

37. Chung, J. *et al.* Molecular modifiers reveal a mechanism of pathological crystal growth inhibition. *Nature* **536**, 446-450 (2016).

38. Diercks, C. S. & Yaghi, O. M. The atom, the molecule, and the covalent organic framework. *Science* **355**, eaal1585 (2017).

39. Ma, W. *et al.* Size-controllable synthesis of uniform spherical covalent organic frameworks at room temperature for highly efficient and selective enrichment of hydrophobic peptides. *J. Am. Chem. Soc.* **141**, 18271-18277 (2019).

40. Pan, F. *et al.* Long-range ordered porous carbons produced from C_{60}. *Nature* **614**, 95-101 (2023).

41. Jin, Y. *et al.* Confined growth of ordered organic frameworks at an interface. *Chem. Soc. Rev.* **49**, 4637-4666 (2020).

42. Luo, X. *et al.* Wrinkled metal-organic framework thin films with tunable

Turing patterns for pliable integration. *Science* **385**, 647-651 (2024).

43. Liu, M. *et al.* Two-dimensional covalent organic framework films prepared on various substrates through vapor induced conversion. *Nat. Commun.* **13**, 1411 (2022).

44. Liu, M. *et al.* Diffusion limited synthesis of wafer-scale covalent organic framework films for adaptative visual device. *Nat. Commun.* **15**, 10487 (2024).

45. Jing, J. *et al.* Scalable production of ultraflat and ultraflexible diamond membrane. *Nature* **636**, 627-634 (2024).

46. Ma, T. *et al.* Diverse crystal size effects in covalent organic frameworks. *Nat. Commun.* **11**, 6128 (2020).

47. Zhan, G. *et al.* Observing polymerization in 2D dynamic covalent polymers. *Nature* **603**, 835-840 (2022).

48. Gruber, C. G., Frey, L., Guntermann, R., Medina, D. D. & Cortés, E. Early stages of covalent organic framework formation imaged in operando. *Nature* **630**, 872-877 (2024).

49. Yi, L., Gao, Y., Luo, S., Wang, T. & Deng, H. Structure evolution of 2D covalent organic frameworks unveiled by single-crystal X-ray diffraction. *J. Am. Chem. Soc.* **146**, 19643-19648 (2024).

50. Wei, L. *et al.* Dimensionality and molecular packing control of covalent organic frameworks through pendant group design. *J. Am. Chem. Soc.* **146**, 31384-31390 (2024).

51. Shen, B. *et al.* Atomic imaging of zeolite-confined single molecules by electron microscopy. *Nature* **607**, 703-707 (2022).

52. Mo, Y.-P., Liu, X.-H. & Wang, D. Concentration-directed polymorphic surface covalent organic frameworks: rhombus, parallelogram, and kagome. *ACS Nano* **11**, 11694-11700 (2017).

53. Chen, C. *et al.* Investigating a seemingly simple imine-linked covalent organic framework structure. *J. Am. Chem. Soc.* **146**, 35504-35512 (2024).

54. Deng, D. *et al.* Catalysis with two-dimensional materials and their heterostructures. *Nat. Nanotechnol.* **11**, 218-230 (2016).

55. Pomerantseva, E. & Gogotsi, Y. Two-dimensional heterostructures for energy storage. *Nat. Energy* **2**, 17089 (2017).
56. Kang, C. *et al.* Covalent organic framework atropisomers with multiple gas-triggered structural flexibilities. *Nat. Mater.* **22**, 636-643 (2023).
57. Ma, Y.-X. *et al.* A dynamic three-dimensional covalent organic framework. *J. Am. Chem. Soc.* **139**, 4995-4998 (2017).
58. Auras, F. *et al.* Dynamic two-dimensional covalent organic frameworks. *Nat. Chem.* **16**, 1373-1380 (2024).
59. Dharmarwardana, M. *et al.* Strong π-stacking causes unusually large anisotropic thermal expansion and thermochromism. *Proc. Natl. Acad. Sci. U. S. A.* **118**, e2106572118 (2021).
60. Xu, H., Gao, J. & Jiang, D. Stable, crystalline, porous, covalent organic frameworks as a platform for chiral organocatalysts. *Nat. Chem.* **7**, 905-912 (2015).
61. Feng, B. *et al.* Isomeric dual-pore two-dimensional covalent organic frameworks. *J. Am. Chem. Soc.* **145**, 26871-26882 (2023).

Methods

Biphasic synthesis of Py-COF polycrystals. For the synthesis of Py-1P polycrystals, $Py(NH_2)_4$ (11.3 mg, 20 μmol) and TPA (5.4 mg, 40 μmol) were dissolved in DCM (10 mL) by ultrasonication at 50 °C to form a homogeneous solution. After cooling to room temperature by water rinsing, the solution was transferred to a glass bottle (3.5 cm in diameter). To this organic solution, an AcOH aqueous solution (6 M, 10 mL) was added to create an organic-aqueous biphasic interface. The glass bottle was capped and left undisturbed at room temperature for designated durations. After completion of the reaction, the product generated in the organic solution was collected by centrifugation and sequentially washed with ethanol, tetrahydrofuran, and n-hexane. The final product was vacuum-dried at 85 °C for 3 h to yield Py-1P polycrystals. AcOH solutions with various molarities were used in parallel experiments to evaluate

the effect of acidity on crystal growth. For the synthesis of the other Py-COF polycrystals, the molar quantities of the corresponding monomers and the procedures followed those used for Py-1P-6-72.

Biphasic synthesis of Py-COF polyhedral films. Prior to film growth, the glass bottle (3.5 cm in diameter) was pretreated by immersion in an alkaline bath overnight, followed by thorough washing and drying. The synthesis procedure of Py-1P polyhedral films was adapted from that used for Py-1P polycrystals. To be specific, $Py(NH_2)_4$ (11.3 mg, 20 μmol) and TPA (5.4 mg, 40 μmol) were dissolved in DCM (10 mL) by ultrasonication at 50 °C to form a homogeneous organic solution. After cooling to room temperature by water rinsing, the solution was transferred to the glass bottle preloaded with substrates such as glass plates, silicon wafers, porous alumina disks, or porous polymer membranes. Then, an AcOH aqueous solution (6 M, 10 mL) was added to the organic solution. The glass bottle was capped and kept undisturbed at room temperature for designated durations. After synthesis, the polyhedral films grown on the substrates were sequentially washed with ethanol, tetrahydrofuran, and n-hexane, and stored in n-hexane before use. The Py-1P polyhedral films formed on the inner walls of the glass bottle were also collected and fully washed before use. For the synthesis of the other Py-COF polyhedral films, the molar quantities of the corresponding monomers and the procedures followed those used for Py-1P films. A 6 M AcOH aqueous solution was used in these cases, with a reaction time of 48 h for Py-G and 72 h for the rest.

Variable-temperature PXRD tests. In situ variable-temperature PXRD patterns of Py-COF polyhedral films were recorded using a Rigaku MiniFlex 600 X-ray powder diffractometer with Cu Kα radiation (λ = 1.5406 Å) coupled with a benchtop heating stage (Anton Paar BTS500). The temperature was ramped from 50 to 350 °C and then decreased back to 50 °C, with a step of 50 °C and a rate of 10 °C min^{-1}. At each target temperature, the system was stabilized for 2 min prior to PXRD measurements. An inert environment was maintained throughout the tests by N_2 purging at a flow rate of 10 mL min^{-1}.

Variable-temperature FTIR tests. In situ variable-temperature FTIR spectra of Py-COF polycrystals were recorded using a Thermo Scientific Nicolet iS50 spectrometer. The temperature was ramped from 50 to 300 °C and then decreased to 0 °C with a step of 50 °C. At each target temperature, the system was stabilized for 10 min prior to FTIR measurements. An inert environment was maintained throughout the tests by N_2 purging at a constant flow rate of 10 mL min^{-1}.

Variable-temperature spectroscopic ellipsometry tests. In situ film thickness and roughness measurements as a function of temperature were performed using a spectroscopic ellipsometer (CompleteEASE M-2000U, J. A. Woollam) equipped with a heating cell (HTC-100). Thickness measurements were performed by analyzing changes in the polarization state of light reflected from the film surface and fitting the data to an optical model. The experiments were conducted at an incidence angle of 70° over a wavelength range of 400-999.8 nm under atmospheric conditions. The temperature was ramped from 50 to 250 °C, with a step of 50 °C and a heating rate of 10 °C min^{-1}. At each target temperature, the system was stabilized by holding the temperature for 1 min. Following the heating process, natural cooling to 50 °C was carried out. A Cauchy transparent film model was used for thickness fitting.

Low-dose HRTEM and iDPC-STEM tests. Low-dose HRTEM imaging was conducted on a double aberration-corrected Thermo Scientific Spectra 300 TEM with a Gatan K3 camera at 300 kV. Using counting and correlated double sampling mode of K3 camera, 60 individual image frames were collected with a total exposure of 4 s. These frames were aligned and superposed using Gatan Digital Micrograph software to improve the signal-to-noise ratio and correct sample drifts during exposure. The total accumulated electron doses for the drift-corrected images were controlled within the range of 10-20 e^- $Å^{-2}$ to minimize beam damage to the samples. iDPC-STEM imaging was performed at 200 kV using a segmented dark-field detector, with a convergence semiangle of 14.9 mrad and collection angles of 16-61 mrad. The probe current was about

1 pA. A high-pass filter was used to reduce low-frequency noises.

Characterizations. SEM measurements were performed on a JEOL JSM-7610FPlus field-emission scanning electron microscope with energy dispersive X-ray spectrometry. The samples were coated with a thin layer of platinum by a Cressington 208 HR sputter coater at 20 mA for 50 s to prevent charging. AFM measurements were performed on a Bruker Dimension Icon AFM microscope under tapping mode. PXRD patterns were recorded on a Rigaku MiniFlex 600 X-ray powder diffractometer with Cu Kα radiation (λ = 1.5406 Å). N_2 sorption tests were performed on a Micromeritics ASAP 2020 surface area and porosity analyzer at 77 K. The samples were activated at 120 °C for about 15 h to reach a vacuum degree of 4 μmHg before measurements. FTIR spectroscopy was performed on a Bruker Vertex 70 spectrometer using an attenuated total reflection method. Raman spectra were obtained using a Renishaw Raman spectrometer with laser excitation at 532 nm at room temperature. Solvent vapor sorption isotherms were tested using a dual balance vapor gravimetric sorption analyzer (DVS Discovery, Surface Measurement Systems). TEM images were recorded on an FEI Talos F200X G2 microscope at 200 kV. ^{13}C NMR spectroscopy was performed on a Bruker Avance 400 MHz NMR spectrometer (DRX400). ^{1}H NMR spectroscopy was tested using a Bruker Avance 400 MHz NMR spectrometer (DRX400). GIWAXS tests were conducted on a Xeuss 3.0 SAXS/WAXS system using a Cu Kα source with a Dectris Eiger2R 1M detector. XPS tests were performed on a Kratos Axis Ultra DLD X-ray photoelectron spectrometer with an excitation source of Al Kα = 1486.71 eV. Thermogravimetric tests were performed on a Shimadzu DTG-60AH analyzer from room temperature to 800 °C with a heating rate of 10 °C min^{-1} under a constant N_2 flow rate of 50 mL min^{-1}.

Acknowledgements

This work was supported by Jiangsu Industrial Technology Research Institute and Nanjing Tech University Membrane Application Institute Co. Ltd. (2020-2210), the Centre for Hydrogen Innovations (CHI-P2024-01), the Ministry of

Education - Singapore (MOE-T2EP10122-0002), the Agency for Science, Technology and Research (U2102d2004, U2102d2012), the National Research Foundation Singapore (NRF-CRP26-2021RS-0002, NRF-NRFI08-2022-0008), the Science and Technology Support Program of Jiangsu Province (BZ2022056), and the National University of Singapore (Suzhou) Research Institute (Energy and Environmental Nanotech Platform). We thank Dr. Anton Tadich from the Australian Synchrotron for his assistance with the NEXAFS tests. This research also used the TEM resources and facilities at the A*STAR Institute of Materials Research and Engineering (A*STAR IMRE).

Author contributions

D.Z. conceived and supervised the project. X.S. synthesized and characterized the polycrystals and polyhedral films and wrote the manuscript. Q.L. prepared the gas sensor devices and conducted sensor performance tests and analyses. H.S. and M.L. performed the low-dose HRTEM and iDPC-STEM tests and analyses. C.K., H.L., J.R., N.Z., W.Z. and Z.Z. contributed to the structural analyses. W.-H.L. and A.M. contributed to the sensor performance analyses. D.S. performed the NEXAFS tests. Y.W. contributed to the variable-temperature spectroscopic ellipsometry tests. All authors discussed the results and contributed to the manuscript. X.S. and Q.L. contributed equally to this work.

Competing interests

The authors declare no competing interests.

Data availability

All the data supporting the findings of this study are available in the Article and its Supplementary Information.